Proceedings of the Fortieth Turbomachinery Symposium
September 12-15, 2011, Houston, Texas

DEVELOPMENT OF ADVANCED CENTRIFUGAL COMPRESSORS AND PUMPS FOR CARBON CAPTURE AND SEQUESTRATION APPLICATIONS

J. Jeffrey Moore, Ph.D.
Program Manager
Southwest Research Institute®
San Antonio, Texas, USA

Tim Allison, Ph.D.
Research Engineer
Southwest Research Institute®
San Antonio, Texas, USA

Andrew Lerche
Sr. Research Engineer
Southwest Research Institute®
San Antonio, Texas, USA

Jorge Pacheco, Ph.D.
Senior Development Engineer
Dresser-Rand
Olean, New York, USA

Hector Delgado
Research Engineer
Southwest Research Institute®
San Antonio, Texas, USA

Dr. Jeffrey Moore is a program manager at Southwest Research Institute in San Antonio, TX. He holds a B.S., M.S., and Ph.D. in Mechanical Engineering from Texas A&M University. His professional experience over the last 20 years includes engineering and management responsibilities related to centrifugal compressors and gas turbines at Solar Turbines Inc. in San Diego, CA, Dresser-Rand in Olean, NY, and Southwest Research Institute in San Antonio, TX. His interests include advanced compression methods, rotordynamics, seals and bearings, computational fluid dynamics, finite element analysis, controls and aerodynamics. He has authored over 25 technical papers related to turbomachinery and has three patents pending. Dr. Moore held the position of Oil and Gas Committee Chair for IGTI Turbo Expo. He is also a member of the Turbomachinery Symposium Advisory Committee, the IFToMM International Rotordynamics Conference Committee, and the API 616 and 684 Task Forces.

Andy Lerche is a senior research engineer at Southwest Research Institute in San Antonio, TX. He holds B.S. and M.S. in Mechanical Engineering from the University of Texas at Austin and the University of Texas at San Antonio, respectively. Over the last 10 years he has worked in areas involving mechanical design, rotordynamic analysis, finite element analysis, computational fluid dynamics, experimental testing, and test rig development. His interests include structural dynamics, modal testing and analysis, fluid-structure interaction, rotordynamics, instrumentation and telemetry, and sustainable/renewable energies.

Hector Delgado is a research engineer at Southwest Research Institute in San Antonio, TX. Mr. Delgado has worked on many projects related to turbomachinery root cause failure analysis, machinery field testing, rotordynamics, and mechanical design and remaining life prediction of mechanical and piping system components. Mr. Delgado studied Mechanical Engineering at the University of Nuevo Leon and received his diploma in 2003. He received a M.Sc. degree from the University of Texas at San Antonio in 2006.

Dr. Tim Allison is a research engineer at Southwest Research Institute in San Antonio, TX, where his research interests include turbomachinery vibrations analysis and testing, performance, blade dynamics, and rotordynamics. Dr. Allison received his M.S. in Aerospace Engineering from the University of Texas at Austin in 2005 and his Ph.D. in Mechanical Engineering from Virginia Polytechnic Institute and State University in 2007 with a focus on structural dynamics system identification.

Dr. Jorge Pacheco is the supervisor of the Aerodynamics-Thermodynamics Design group for Dresser-Rand in Olean, New York. His team is involved in new centrifugal compressor stage development, multi-phase modeling for gas-liquid separation, full-scale and sub-scale testing, and axial compressor and turbine product development support. Dr. Pacheco received his B.S. degree (mechanical engineering, 1997) from Universidad Simon Bolivar, M.S. (mechanical engineering, 2000) and Ph.D. degrees (mechanical engineering, 2003) from Carnegie Mellon University. Before joining Dresser-Rand, Dr. Pacheco was a professor at Universidad Simon Bolivar for three years in the

Thermodynamics and Transport Phenomena Department. Dr. Pacheco is a member of ASME.

ABSTRACT

In order to reduce the amount of carbon dioxide (CO_2) greenhouse gases released into the atmosphere, significant work has been made in sequestration of CO_2 from power plants and other major producers of greenhouse gas emissions. The compression of the captured CO_2 stream requires significant power, which impacts plant availability, capital expenditures, and operational cost. Preliminary analysis has estimated that the CO_2 compression process alone reduces the plant efficiency by 8-12 percent for a typical power plant. The goal of the present research is to reduce this penalty through development of novel compression and pumping processes. The research supports the U.S. Department of Energy (DOE) National Energy Technology Laboratory (NETL) objectives of reducing the energy requirements for carbon capture and sequestration in electrical power production. However, the technology presented here is applicable to other gases including hydrocarbons as well as smaller scale carbon capture projects including CO_2 separation from natural gas. The primary objective of this study is to boost the pressure of CO_2 from near atmospheric to pipeline pressures with the minimal amount of energy required. Previous thermodynamic analysis identified optimum processes for pressure rise in both liquid and gaseous states. Isothermal compression is well known to reduce the power requirements by minimizing the temperature of the gas entering downstream stages. Intercooling is typically accomplished using external gas coolers and integrally geared compressors. Integrally geared compressors do not offer the same robustness and reliability as in-line centrifugal compressors. The current research develops an internally cooled compressor diaphragm to remove heat internal to the compressor. Results documenting the design process will be presented including 3-dimensional (3D) conjugate heat transfer computational fluid dynamics (CFD) studies. Experimental demonstration of the design was performed using a centrifugal compressor closed loop test facility at the authors' company. A range of operating conditions was tested to evaluate the effect on heat transfer. At elevated pressures, CO_2 assumes a liquid state at moderate temperatures. This liquefaction can be achieved through commercially available refrigeration schemes. However, liquid CO_2 turbopumps of the size and pressure needed for a typical power plant were not readily available. This paper describes the test stand design and construction as well as the qualification testing of a 150 bar cryogenic turbopump. A range of suction pressures were tested and net positive suction head (NPSH) studies were performed.

INTRODUCTION

In the effort to reduce the release of CO_2 greenhouse gases to the atmosphere, sequestration of CO_2 from Integrated Gasification Combined Cycle (IGCC), Oxy-Fuel, and Pulverized Coal (PC) power plants is being pursued. This approach, however, requires significant compression power to boost the pressure to typical pipeline levels. According to (Herzog, 1997), the power penalty for carbon capture can be as high as 27-37 percent for a traditional PC power plant and 13-17 percent for a typical IGCC plant. The compression represents a significant percentage of this total.

The goal of this research is to reduce this penalty through novel compression and pumping concepts by developing concepts to boost the pressure of CO_2 to pipeline pressures with the minimal amount of energy required. Fundamental thermodynamics were studied to explore pressure rise in both liquid and gaseous states. In addition to compression options, liquefying CO_2 and liquid pumping were explored as well. Thermodynamic studies, by (Moore and Nored, 2008), indicated that a reduction in power up to 35 percent is possible by a combined compression/pumping solution including the cost of liquefaction when combined in series with isothermal compression. Figure 1 shows a schematic of this concept. The proposed compressor contains internal cooling to remove the heat of compression and the pressure is boosted to around 250 psi. The flow is passed through an economizer where heat is transferred to the refrigerated liquid stream exiting the pump. A vapor-compression refrigeration system is used to liquefy the CO_2 at its saturation temperature of -10°F, which is well within the temperature range for these systems. The stream is collected in a vessel and fed to a multi-stage centrifugal pump where the pressure is boosted to pipeline levels near 2,200 psi.

Isothermal compression can be accomplished with an integrally geared type of machine where multiple pinions are driven off of a common bull gear. Up to 10 stage of compression is possible with this arrangement. However, reliability of integrally geared compressors cannot match the in-line centrifugal machines so widely used in the oil and gas industry. Therefore, this research seeks to design an internally cooled, in-line centrifugal compressor diaphragm that removes the heat of compression without the need for external intercoolers using liquid cooling. Significant challenges exist in cooling a high velocity gas internal to the compressor, such as limited surface area and minimizing pressure drop of the gas stream. By utilizing 3D CFD, an optimal design was achieved that provides good heat transfer while adding no additional pressure drop. A single-stage prototype diaphragm was built and tested to determine both aerodynamic and heat transfer performance.

A turbopump in this pressure and flow range, required for sequestration, is not readily available in the market place. Therefore, this paper also describes an experimental test loop that was designed and constructed to perform qualification tests of a multi-stage turbopump originally designed for liquid nitrogen and liquefied natural gas (LNG) service. Performance and mechanical test data were gathered and will be presented according to (ASME PTC 8.2, 1990).

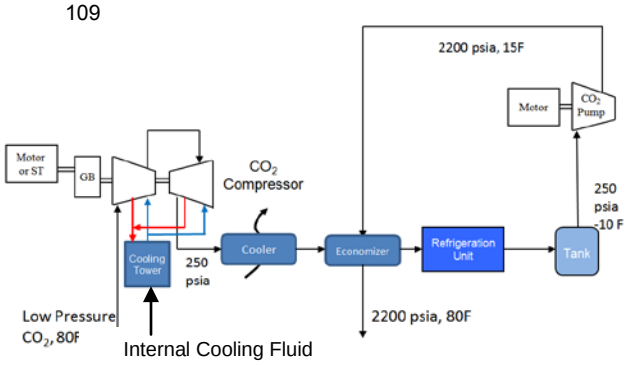

Figure 1. Schematic of Combined Compression/ Pumping Concept

COMPRESSOR DESIGN CONCEPT

This section describes the development of an internally-cooled compressor diaphragm (patent pending) that removes heat of compression between each impeller. Figure 2 shows the conceptual design where cooling flow (blue) is routed through the diaphragms adjacent to the gas flow path (red). The total temperature increases, due to the work input of the impeller, are reduced through the diaphragm flow path thereby reducing the temperature into the downstream stage. An efficient heat transfer mechanism is necessary to ensure that the compression process is near isothermal. Various heat transfer enhancement techniques have been reported in the open literature. A comprehensive literature survey was performed and the feasibility of those reported techniques was assessed.

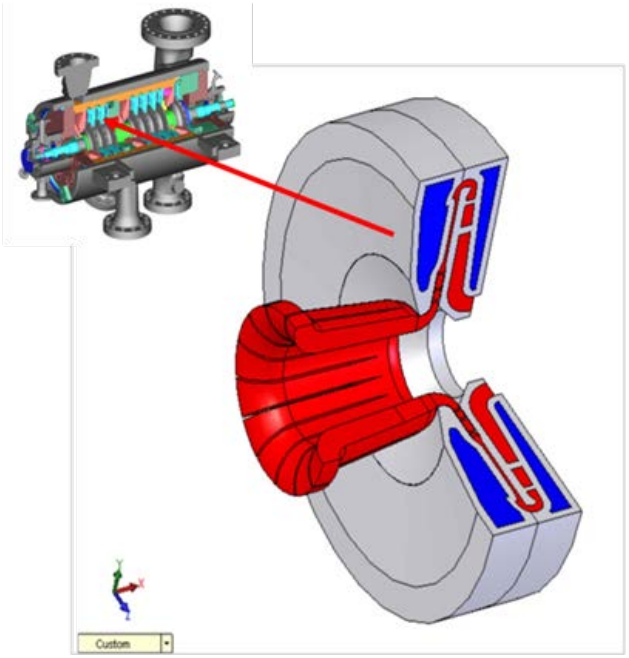

Figure 2. Cooled Diaphragm Concept

CONJUGATE HEAT TRANSFER CFD MODELS

Conjugate heat transfer (CHT) CFD models were developed that combined the diaphragm structure, cooling fluid, and the diaphragm process gas flow path. A 1/12th section model was utilized for all the models (see Figure 3).

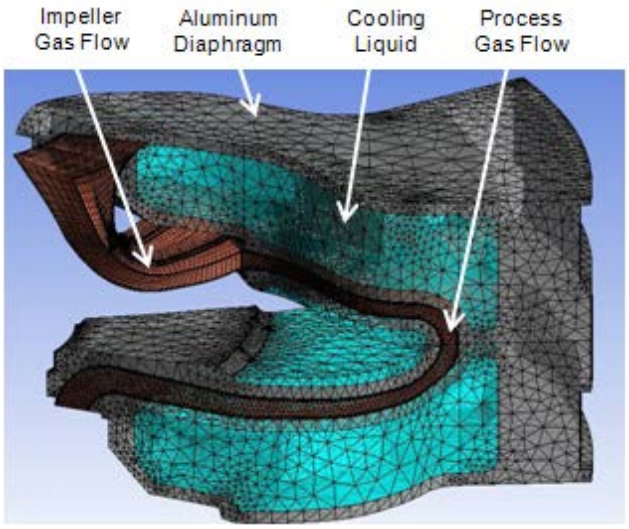

Figure 3. Grid from Conjugate Heat Transfer Section Model

The CHT model was developed in three main steps. The first step developed a CFD model that included only the process gas with adiabatic boundaries. The second step developed a heat transfer model that included the process gas and the diaphragm. This model included the heat transfer between the process gas and the diaphragm. A heat transfer coefficient that simulates the heat transfer between the cooling fluid and diaphragm was calculated and applied to the diaphragm boundaries. The third CFD model consisted of the full CHT model, which included the process gas, the diaphragm, and the cooling fluid. These models are described below.

Adiabatic CFD Model Results

The adiabatic model showed relatively good correlation with the test data, as seen in Table 1. The difference with the OEM data was due to the fact that the additional losses in the inlet and volute were not accounted for in the CFD model. A close match of the work input (power) was demonstrated.

Table 1. CFD Model Comparison to Test Results

	OEM Data	Model	(%) Difference
Total Pressure Ratio	1.550	1.648	6.3
Total Temperature Ratio	1.136	1.139	0.3
Gas Power [HP]	102.0	104.3	2.3

Conjugate Heat Transfer Model with Coefficients

The CHT model that used calculated heat transfer coefficients at the boundaries modeled the heat transfer between the diaphragm and cooling liquid. These coefficients were calculated assuming a total cooling liquid flow of about 20 gallons per minute (gpm). The following equations show how the heat transfer coefficients were determined:

$$h = Nu_D \frac{k}{D_H} \quad (1)$$

where Nu_D is the Nusselt number for a smooth wall channel and was defined by

$$Nu_D = \frac{\frac{f}{8}(Re_D - 1000)Pr}{1+12.7\left(\frac{f}{8}\right)^{\frac{1}{2}}\left(Pr^{\frac{2}{3}}-1\right)} \text{ for } \begin{bmatrix} 3000 \leq Re \leq 5\times10^6 \\ 0.5 < Pr < 2000 \\ \left(\frac{L}{D}\right) \geq 10 \end{bmatrix} \quad (2)$$

where f is the friction factor for a smooth surface condition and was defined by

$$f = (0.790 \ln Re_D - 1.64)^{-2} \quad (3)$$

and Re_D is the Reynolds number and was defined by

$$Re_D = \frac{\rho u_m D_H}{\mu} \quad (4)$$

where D_H is the hydraulic diameter and was defined by

$$D_H = \frac{4A_c}{P} \quad (5)$$

The mean fluid velocity was represented by u_m, μ was the dynamic viscosity of the fluid, and k was the thermal conductivity of the fluid. A_c was the cross sectional area of the passage, P was the perimeter, and ρ was the fluid density. The Prandtl number of water was approximately

$$Pr = 4.62 \text{ for water at } 116°F. \quad (6)$$

Full Conjugate Heat Transfer Model with Cooling Liquid

A CHT model was developed with water as the cooling fluid at a supply rate of 20 gpm. This model had the cooling fluid flowing in the opposite direction as the process gas, as in counter flow heat exchangers.

To simulate the cooling flow in the pie-section CFD model, an inlet for the cooling flow was specified for each main passage. Figure 4 shows the velocities specified in the CFD model. The flow rate decreases at the outlet (upper plenum) due to the cooling flow passing to the opposite plenum.

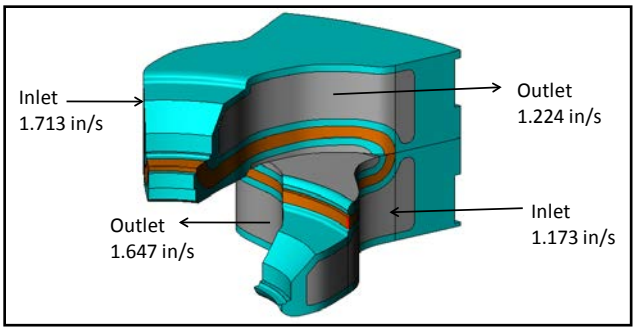

Figure 4. Flow Boundary Conditions for Cooling Fluid

Summary of CFD Results

The two CHT models compared very well with each other and were also compared with the adiabatic case in Table 2, which compares the total temperature and pressure ratios to the impeller exit and the entire stage. The impeller was modeled as two 1/19th sections and the stator was modeled as two 1/24th sections. The impeller temperature ratio is identical for all cases since the heat transfer occurs downstream of the impeller. The two CHT models showed less than one percent difference in temperature and pressure change from inlet to stage outlet. This demonstrates that calculated heat transfer coefficients effectively simulated the cooling flow. Also, the two CHT models showed the improvement from cooling with a stage outlet temperature approximately 13°F less than the adiabatic case.

Table 2. CFD Results of Adiabatic and Conjugate Heat Transfer Models

Model	Quantity	Impeller Ratio	Stage Ratio
Adiabatic	Total Pressure	1.773	1.670
	Total Temperature	1.142	1.142
Diabatic with Heat Transfer Coefficients	Total Pressure	1.764	1.671
	Total Temperature	1.141	1.116
Diabatic with Full Conjugate Heat Transfer	Total Pressure	1.767	1.678
	Total Temperature	1.141	1.117

Enhanced Conjugate Heat Transfer Models

Several CHT models were also developed that included heat transfer enhancements, such as dimpled surfaces, ribs, etc. The heat transfer enhancement on the liquid side assumed ribbed surfaces and used increased heat transfer coefficients based off the literature to simulate the enhancements (Han, 2006). The heat transfer enhancement on the gas side assumed dimpled surfaces on the diaphragm surfaces, and parallel groove enhancements on the blades. The dimple pattern is intended to provide increased heat transfer without adding significant pressure drop (Ridouane and Campo, 2008). The radius ratio, which is defined as the radius to the outside of the diffuser divided by the impeller radius, was maximized to increase heat transfer surface area and improve flow diffusion.

Figure 5 presents a meridional view showing the predicted total temperature distribution through the passage and demonstrates the temperature reduction throughout the stationary flow path of the stage.

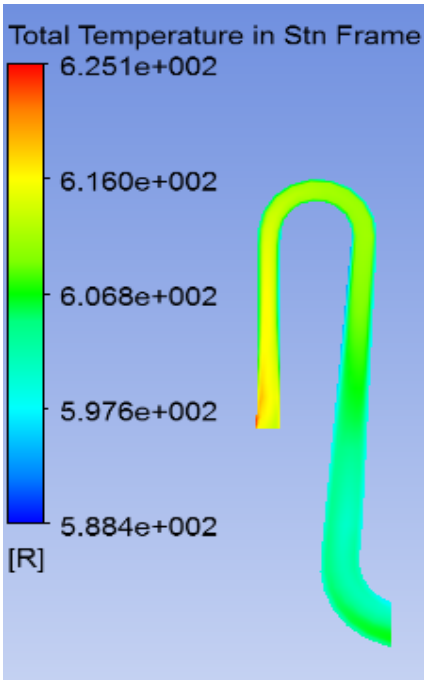

Figure 5. Meridional View of Total Temperature Distribution

CO_2 Compressor One-Dimensional Thermodynamic Calculations

As only a single stage is being tested, a predictive tool was developed that would estimate power consumption of a multi-stage compressor based on CFD results from a single stage. This tool used pressure loss, pressure ratio, and heat transfer predictions from a CFD analysis of a single stage to predict power savings for multiple stages. The tool used one-dimensional (1D) isentropic equations combined with a calibrated equation of state for CO_2 and 1D energy balance equations. Values for stage isentropic efficiency, stage heat exchanger effectiveness, and return channel pressure loss were first analytically determined, and then empirically calibrated using CFD data. The calculations set the inlet pressure to the compressor at 30 psia and fixed the output pressure at 250 psia. Head rise across each stage was assumed to be constant, and altered for each case until the required output pressure was achieved.

The following cases were run to compare power savings:

Adiabatic – No heat transfer from CO_2, serves as the baseline for other cases.

Smooth wall (SW) heat transfer – Smooth walls on both the water and CO_2 sides, i.e., no convection coefficient augmentation geometry used.

Smooth wall heat transfer at 9,155 rpm – Same smooth wall geometry, as previous case; however, operated with a reduced stage pressure ratio to simulate a slower speed.

Smooth wall with higher radius ratio – In order to increase heat exchanger effectiveness, surface area was increased by using a longer return channel.

Ribbed water side walls and dimpled CO_2 side walls – A convection coefficient augmentation case.

Ribbed water side walls, dimpled CO_2 side walls, and grooved airfoils – The second convection coefficient augmentation case.

It was found that despite an increased reduction in CO_2 temperature, convection coefficient augmentation geometry on the gas side offered very small power savings. This was due to the fact that the benefit of low gas temperature was matched by increased total pressure losses. In a low pressure ratio stage, where temperature and pressure rise is relatively small, increasing pressure losses in the return channel has a significant impact on power consumption. A significant rise in pressure loss occurs for the augmentation geometry cases (gas-side) which offsets some of the benefit of heat transfer.

The power consumption results are summarized in Table 3. Note that for the 9,155 rpm case, nine stages were required to achieve the required discharge pressure as opposed to five for the 12,850 rpm cases. It is believed that the increased power savings of the 9,155 rpm case was due to the increase in heat exchanger surface area. Running any of the other cases at a slower speed (and more stages) would produce a similar effect.

As was expected, the larger radius ratio case had a power savings advantage over the low radius ratio case, due to more heat exchanger surface area and better diffusion. Based on the results, it would be most advantageous to use the high radius ratio with more stages running at a reduced pressure ratio, if possible. Combining the lower speed with the high radius ratio should result in a power savings greater than 20 percent.

Table 3. Summary of Power Savings with Respect to Adiabatic Case

Geometry	Speed (rpm)	Radius Ratio	Power Savings (%)
Adiabatic Reference	12850	Low	0
Smooth Wall	12850	Low	9.5
Smooth Wall	9155	Low	16.6
Smooth Wall	12850	High	12.3
Ribs and Dimples	12850	Low	4.3
Ribs, Dimples, and Grooves	12850	Low	2.4

COMPRESSOR DIAPHRAGM MANUFACTURING

The original plan was to cast the cooled diaphragms using a sand cast process that creates the mold using rapid prototyping. However, despite extensive work with the casting vendor, including several iterations with the design, the process could not support the thin walls necessary in the diffuser vane locations. Therefore, the design was modified to permit fabrication by first machining the individual components, welding the pieces together, heat treating, and final machining the weldment. Figure 6 shows the assembled parts of one diaphragm half prior to welding.

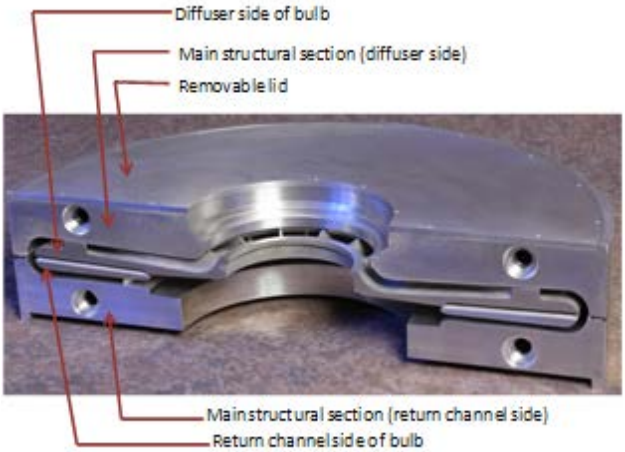

Figure 6. Un-welded Diaphragm Half

COMPRESSOR LOOP ASSEMBLY AND INSTRUMENTATION

The compressor diaphragm was installed into the compressor casing, and instrumentation was installed in the diaphragm and throughout the test loop. Final machining was performed on the diaphragm lids to allow for instrumentation, and the rotor was assembled with seals and bearings. A photograph of the rotor and bottom half of the diaphragm is shown in Figure 7. Both adiabatic (no cooling) and diabatic (with cooling) tests were performed. The assembled compressor (with compressor casing still open) is shown in Figure 7 and the compressor drive train in Figure 8.

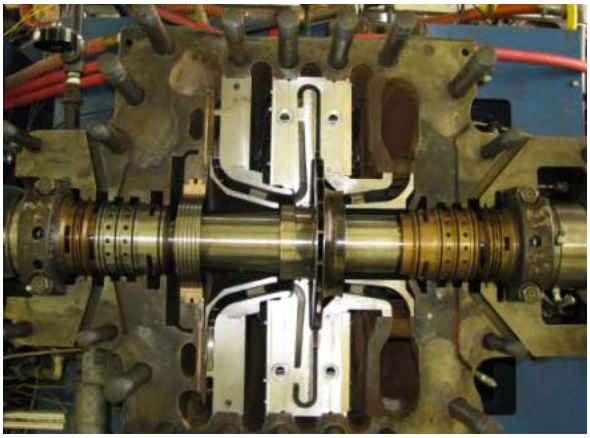

Figure 7. Rotor and Diaphragm Installed in Casing

Figure 8. Compressor Drive Train

DATA ACQUISITION AND INSTRUMENTATION

Multiple pressure and temperature sensors were installed at various stations throughout the flow path. An end-to-end calibration of all temperature probes was performed prior to installing the probes inside the loop and diaphragm. All sensors were then installed in their locations, and probes inside the compressor flow path were oriented towards the local flow path angle predicted by CFD analysis. A photograph of a combination Kiel head pressure and temperature probe in the suction bridge-over is shown in Figure 9, and a half-shielded thermocouple probe installed near the impeller exit (actually just downstream of the diffuser vane leading edge) is shown in Figure 10. Finally, cables for all of the internal instrumentation were passed through the compressor casing via sealing glands. The top of the compressor casing after final assembly is shown in Figure 11, where gland seals permit the pressure tubing and thermocouple wires to pass through the case. The case penetrations for the cooling water inlet and outlet are also shown.

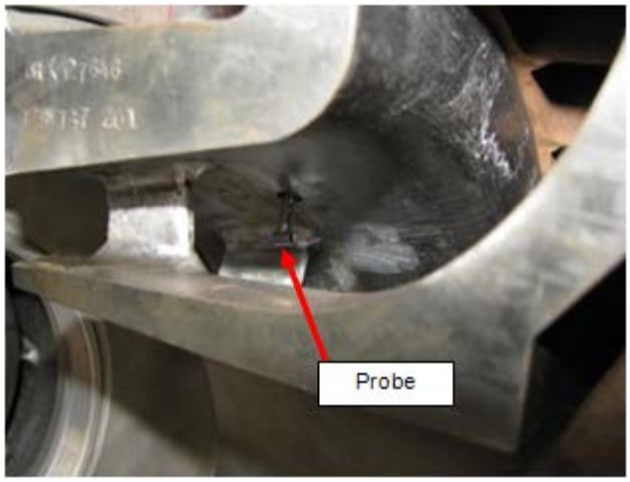

Figure 9. Combination Kiel Head Pressure/Temperature Probe at Suction Bridge-over

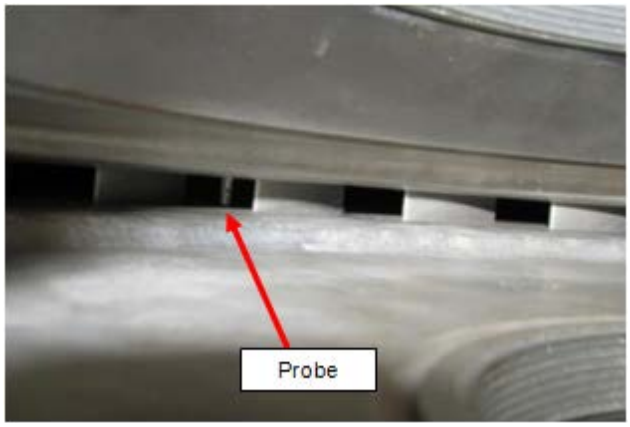

Figure 10. Half-Shielded Thermocouple Probe near Impeller Exit

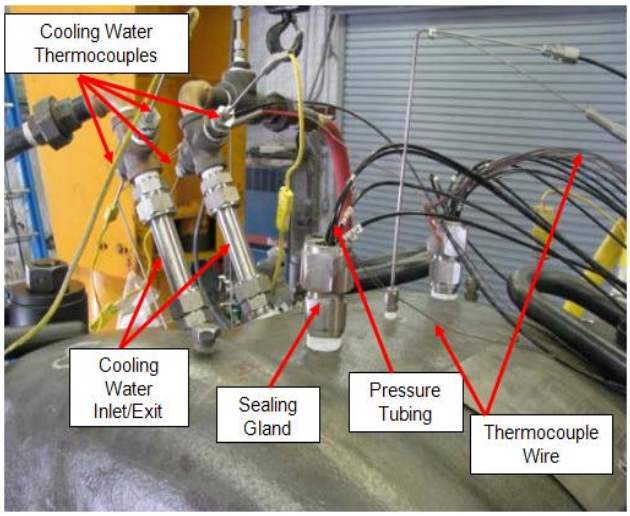

Figure 11. Instrumentation Cables Exiting Compressor Casing

The data acquisition and loop control software for the CO_2 compressor loop was developed using LabVIEW-based software and was capable of sending and receiving data to and from both PSI NetScanner 9116 pressure scanners and National Instruments CompactDAQ systems in order to control and monitor the test rig. The program captured, displayed, and saved raw data measurements to a data log file at 0.5-second intervals (0.5-second data were acquired at 1 kHz and averaged every half second). In addition, real-time performance calculations were performed, and the results were displayed during 0.5-second intervals. Finally, the program also allowed performance snapshots to be taken at the user's request. In order to form a data snapshot, raw data were captured and averaged for a 10 second period, and then performance calculations were performed on the averaged raw data. Snapshots were also saved to a file.

The program interface consisted of 10 main tabs. The "Main Screen" tab, shown in Figure 12, consisted of a display of performance results (head, flow, power, efficiency, etc.) in the upper left corner, a head/flow map in the upper right corner, and buttons for importing a predicted compressor performance map and recording data snapshots in the lower right corner. In the lower left corner, there were alarm indicators for bearing temperatures, lube oil pressures and temperatures, and buffer gas pressure differential. Finally, speed and throttle valve controls were located in the lower middle area of the tab.

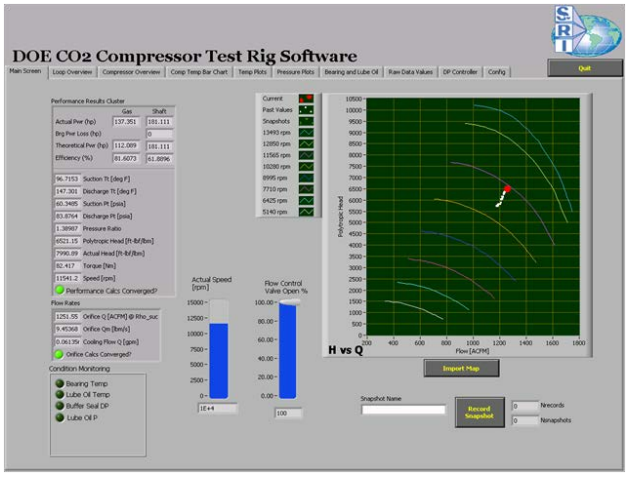

Figure 12. Main Screen of Data Acquisition Code

COMPRESSOR PERFORMANCE CALCULATIONS

After the mass flow rates were determined, the temperature measurements at various locations inside the compressor were converted to total temperatures. The flow velocity at the suction and discharge measurement locations was used to calculate the total temperature and pressure at these locations using procedures based on those in (ASME PTC-10, 1997), Section 5.4. This conversion procedure was also performed for temperature measurements at the impeller exit, diffuser vane exit, and return channel bend. Stage performance was calculated at the bridge-over locations in order to eliminate the effect of the inlet and exit collector. This approach better

represents a central stage in a multi-stage compressor.

Heat Exchanger Performance

This section discusses the methodology for computing the heat transfer performance of the cooled diaphragm. The heat transfer effectiveness was calculated using the effectiveness-NTU method (Cengel, 2003), where dimensionless heat transfer effectiveness is defined as

$$\varepsilon = \frac{\dot{Q}}{\dot{Q}_{max}} = \frac{Actual\ Heat\ Transfer\ Rate}{Maximum\ Possible\ Heat\ Transfer\ Rate} \quad (7)$$

The actual heat transfer rate was computed from either the water or the CO_2 as

$$\dot{Q} = C_{H2O}\left(T_{H2O,out} - T_{H2O,in}\right) = C_{CO2}\left(T_{CO2,in} - T_{CO2,out}\right) \quad (8)$$

where $C_{H2O} = \dot{m}_{H2O}C_{p,H2O}$ and $C_{CO2} = \dot{m}_{CO2}C_{p,CO2}$ were the heat capacity rates of the cooling water and CO_2, respectively. Since all of the data points in Equation (8) were measured, the actual heat transfer rate was calculated as the average value determined from both the water and the CO_2.

The maximum heat transfer rate was defined as

$$\dot{Q}_{max} = C_{min}\left(T_{CO2,in} - T_{H2O,in}\right) \quad (9)$$

where C_{min} was the smaller heat capacity rate of the two fluids. In this case, C_{CO2} was always smaller than C_{H2O}. The above definition is the maximum heat transfer rate because it considers the case when the CO_2 is cooled to the inlet temperature of the water.

COMPRESSOR TEST RESULTS

Performance tests were completed at three speeds (10280, 11565, and 12850 rpm), three cooling flow rates (0, 12, and 20 gpm), and two cooling water temperatures over a range of compressor flows. Adiabatic refers to no heat transfer (no cooling water flow) while diabatic is with cooling. In order to calculate compressor efficiency and heat exchanger effectiveness, it was necessary to use impeller temperature ratios and bearing and windage loss calculations from adiabatic tests. Since this program tested only a single stage compressor, the aerodynamic work input (and power) remained the same between the adiabatic and diabatic (with cooling) tests. Note that the benefit of the cooled diaphragm is realized on downstream stages in a multi-stage compressor.

The measured performance curves for normalized polytropic head and efficiency versus normalized flow are shown in Figure 13 and Figure 14, respectively, for a suction pressure of 30 psia. The values shown are normalized with respect to predicted performance at the design point of the compressor. From these curves it can be seen that the tests captured most of the compressor map (including the design point). The high-flow side of the map could not be measured due to the pressure drop of the loop piping. The measured head versus flow map shows that for adiabatic tests, the measured head versus flow points lie mainly along the predicted curves. It was possible to throttle the compressor to flow values lower than the predicted surge line without encountering surge.

During diabatic tests (with cooling), the head dropped slightly. The measured efficiency versus flow curves (Figure 14) only show the adiabatic test results as compared to predictions. The measurements showed higher efficiency than predicted for adiabatic tests. This discrepancy was likely due to the fact that efficiencies presented from the test data were from the suction bridge-over to discharge bridge-over (stage only) and did not account for inlet and discharge losses that were present in the predicted curves (flange-to-flange). The best efficiency point at the design speed of 12,850 rpm matched the predictions well.

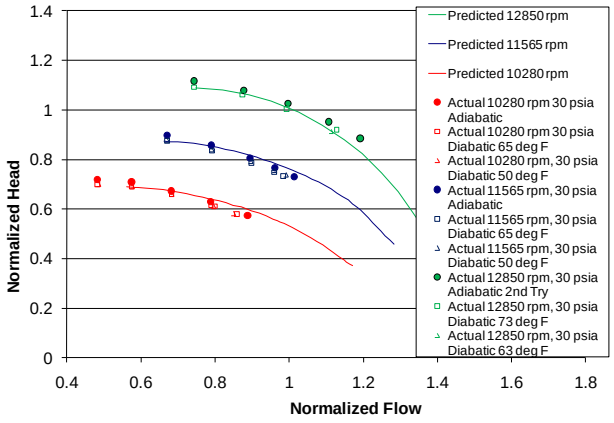

Figure 13. Measured Polytropic Head versus Flow at 30 psia Suction Pressure

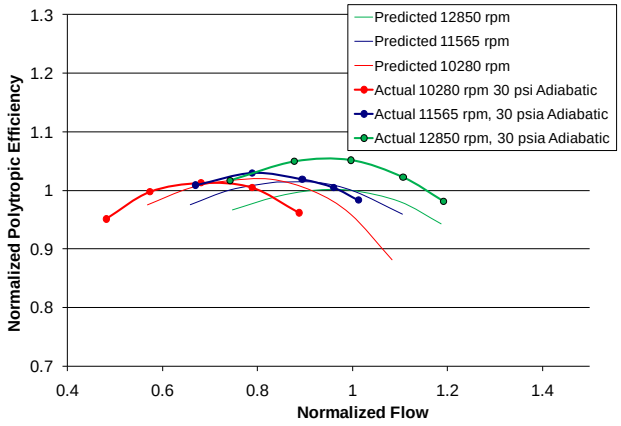

Figure 14. Measured Polytropic Efficiency versus Flow at 30 psia Suction Pressure

The normalized temperature profiles during adiabatic and diabatic tests are shown in Figure 15. This figure illustrates how measured total temperature downstream of the impeller was roughly constant during the adiabatic tests (as expected) but decreased significantly when cooling flow was applied. In some cases, the gas flow temperature decreased by over 20°F, demonstrating the effectiveness of the cooled diaphragm concept. The heat transfer effectiveness is plotted against gas flow rate for the diabatic runs at 30 psia in Figure 16. This figure indicates that heat transfer effectiveness decreased some at higher gas flows and at higher pressures. The heat transfer effectiveness appeared to be insensitive to speed when considering the high speed data was at a slightly higher cooling water temperature. Chilling the water from 65 to 50°F resulted in slightly lower heat exchanger effectiveness.

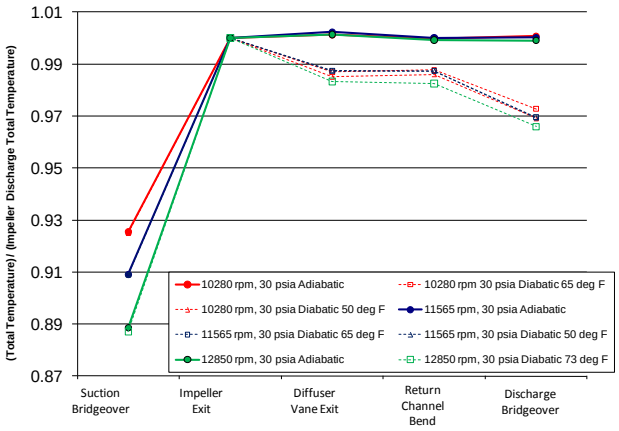

Figure 15. Measured Total Temperature Profiles

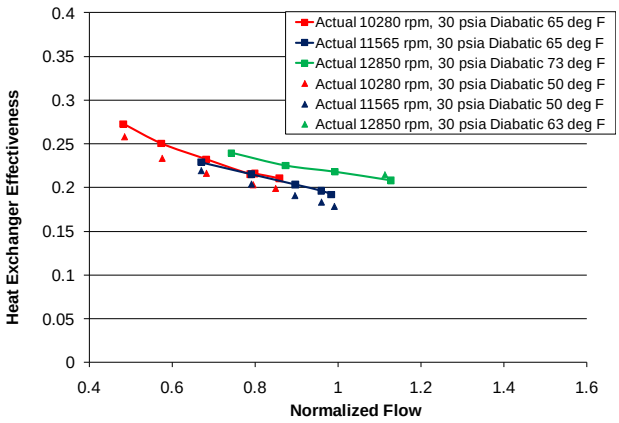

Figure 16. Measured Heat Exchanger Effectiveness versus Flow at 30 psia Suction Pressure

Compressor Testing Measurement Uncertainty

An uncertainty analysis was performed to determine the uncertainty in calculated performance values due to uncertainty in measured data. The uncertainty in each measurement was divided into two categories: calibration uncertainty and measurement uncertainty. Calibration uncertainty was estimated from calibration data from each probe when available (e.g., DP sensor and thermocouples) or from probe specifications (e.g., 0.05 percent full scale error on the pressure scanner). Measurement uncertainty was defined as the uncertainty in the measured value due to variation over multiple time and spatial samples. Each measurement was acquired 20 times (at 2 Hz) and averaged for performance calculations. Thus, at a minimum, 20 samples were used to calculate the standard deviation in a measurement. At some locations, up to four redundant measurements were taken, resulting in 80 samples. The uncertainty is calculated in each measurement for adiabatic and diabatic operation at the design flow (speed = 12,850 rpm) at 30 psia suction pressure. The mean and standard deviation of each data point were used with SwRI's NESSUS™ probabilistic analysis software in order to calculate the resulting uncertainty in performance parameters. For this exercise, an ideal gas model was used for performance calculations (uncertainties calculated in this manner are assumed to be accurate for real gas calculation methodology as well). The probabilistic analysis was performed via the Monte Carlo method with 100,000 samples. The uncertainty results are shown in Table 4 along with the calculated values for each parameter (from calculations using real gas properties). The values are normalized with respect to the predicted values at the design point.

Table 4. Standard Deviations for Measured Values

Quantity	Adiabatic		Diabatic (12gpm, 73°F inlet T)	
	Calculated Value	Standard Deviation	Calculated Value	Standard Deviation
Normalized Flow at Suction Total Conditions	0.9919	0.005547	0.9929	0.004002
Normalized Polytropic Head	1.049	0.01812	1.005	0.01734
Normalized Actual Head	0.9955	0.0371	0.9913	0.0371
Normalized Polytropic Efficiency	1.054	0.04359	1.013	0.04235
Heat Exchanger Effectiveness	N/A	N/A	0.218	0.025
Temperature Reduction Fraction	N/A	N/A	0.302	0.032

Temperature Drop Comparison to CFD Predictions

Plots were made to compare the experimental total temperature and static pressure profiles of the test results and CFD. The total temperature plot is shown in Figure 17. The CFD results followed the same trends as the test results for the temperature on both the adiabatic and diabatic cases. The results are normalized with impeller exit temperature, since the same inlet temperature could not be maintained during the test (CFD used 80ºF) due to higher ambient temperatures that day.

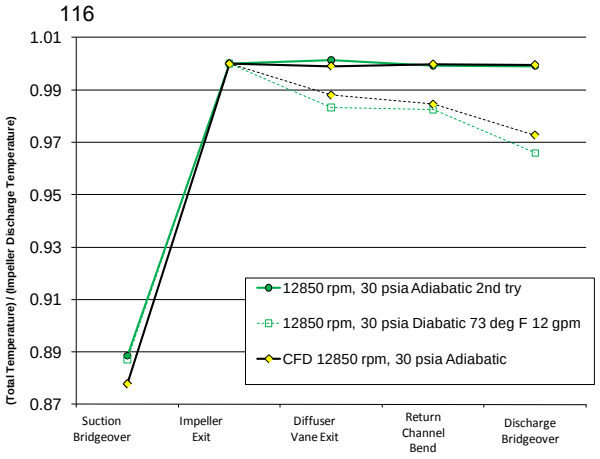

Figure 17. Total Temperature Comparison of CFD and Test Results

Heat transfer effectiveness from the CFD model was compared to the test data. Only one flow condition was modeled with the CFD analysis, thus, there was only one point to compare to the test data. Figure 18 shows the heat transfer effectiveness, assuming 70°F at the cooling liquid inlet, for the CFD case. The experimental runs varied from 65 to 73°F. The CFD prediction, overall, correlated well to the test results. The measured heat exchanger effectiveness actually exceeded the prediction slightly.

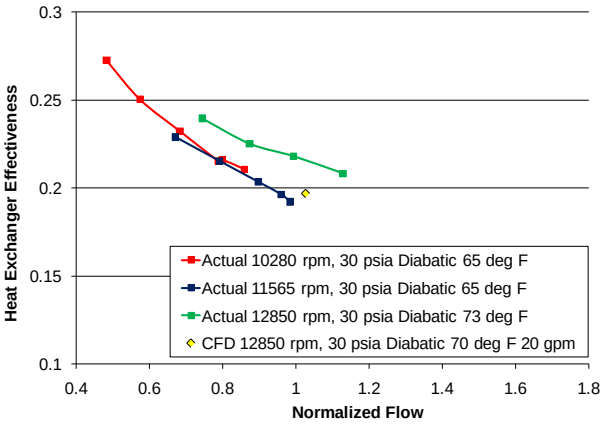

Figure 18. Heat Transfer Effectiveness of CFD and Test Results

DESIGN OF PUMP TEST FACILITY

Next, the pump test rig will be described, which consists of a newly constructed liquid CO_2 test loop and a commercial multi-stage turbopump. The pump is the smallest frame size for this product line but still retains the same configuration as large scale pumps that would be used for power plant applications. The smaller size was selected to keep the cost of the facility to a minimum, yet still provide valid performance and mechanical data. A schematic of the loop is shown in Figure 19.

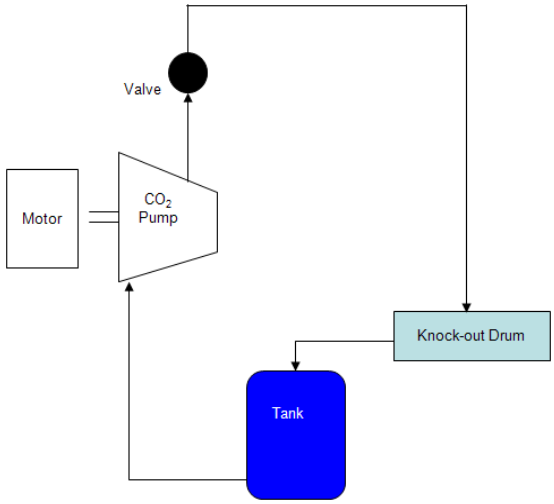

Figure 19. Schematic of Liquid CO_2 Pump Loop

The pump loop consists of a 12-stage pump driven by a variable speed electric motor. The pump parameters are shown in Table 5 and demonstrate the motivation for the smaller scale pump unit. Notice that the flow is about 1/9 of the full scale while the head requirements are identical.

Table 5. Summary of Sub-Scale Pump Parameters

	Full Scale	Test Scale
Power hp (kW)	1807 (1348)	200 (149)
Flow gpm (lpm)	968 (3663)	107 (405)
Head ft (m)	4230(1290)	4230(1290)

The size of the loop components and the power requirements are driving the test scale design. The pump is fed from a 1,000-gallon pressurized vessel that maintains liquid CO_2 at its boiling temperature of -12°F at 250 psia. The discharge of the pump will feed an orifice flow meter run followed by a control valve that will drop the pressure from 2,215 psia down to 250 psia. The control valve will discharge into a knock-out drum for liquid/gas separation, since some flashing of the gas back to the vapor phase will occur. Finally, the liquid CO_2 will be returned to the main vessel through a drain line and the remaining gaseous CO_2 will be vented to the atmosphere through a back pressure control valve.

The pump test will measure pump performance to quantify the power requirements. Also, mechanical performance, including vibration, temperatures, and seal flows, will be quantified. The test rig will be monitored for any sign of cavitation. A NPSH test will be performed in accordance with the (ASME PTC 8.2, 1990) performance test code.

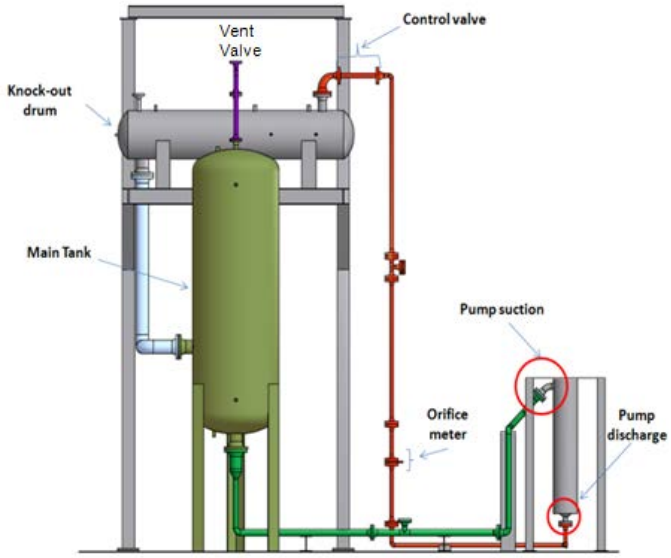

Figure 20. Front View of Loop Solid Model

CONSTRUCTION OF TEST FACILITY

The pilot scale test facility consists of a newly constructed liquid CO_2 test loop and a custom developed test-scale multi-stage pump. The piping was designed using the (ASME, B31.3, 2002). Twenty percent of the welds in the test loop were subjected to and successfully passed X-ray testing. The test loop discharge piping was fabricated using threaded joint connections. The test loop piping and major components were insulated to reduce the amount of heat transfer to the test loop and reduce hazard due to the expected low operating temperature. The pump was installed and electrical connections were made to an 850 kW variable frequency drive (VFD) and all instrumentation is installed. Figure 21 shows a picture of the test loop. A seal control panel is being used to provide conditioned CO_2 for the gas seal and provide conditioned purge gas for the protection chambers inside the pump.

Figure 21. Photo of CO_2 Pump Test Loop

DESCRIPTION OF TEST PUMP

The pump used in this test program is a 12-stage centrifugal cryogenic turbopump mounted in a vertical orientation with a design speed of 3,510 rpm with an impeller diameter of 240 mm. The pump is direct driven by a 250 kW induction motor. A dry gas seal is used to seal the shaft end and is supplied by gaseous CO_2 from bottles through the seal gas control panel. This panel regulates the seal gas at three bars above suction pressure and monitors the flow rate to the seal. The pump is also equipped with a heater to ensure that the pump bearing temperature remains within limits. Bearing temperature and seal gas delta-P is monitored by the data acquisition and control system. The pump has a 0.5 m NPSH requirement at the design point. The behavior of the pump at low NPSH values will be investigated. The pump comes with a support frame and is weather proof.

PUMP PERFORMANCE CALCULATIONS

This section provides results from two separate tests, which will be referred to as Tests 1 and 2. The flow calculations were performed per (API 14.3.4, 2002) for an orifice in liquid flow and head calculations were performed with static and dynamic head as shown below:

Mass flow is calculated in accordance with (API 14.3.4, 2002) standard using the following Equation (10):

$$q_m = \frac{\pi}{4} N_c C_d Y d^2 \sqrt{\frac{2\rho_{t,p}\Delta P}{1-\beta^4}} \quad (10)$$

Since the pressure drop across the orifice plate is minimal compared to the absolute pressure and the stream is single phase, the constant density assumption used in Equation (10) is valid (i.e., Y=1.0).

The pump head is calculated from pressure measurements at the pump suction and discharge locations. The calculation also involves densities obtained from liquid property data for CO_2 provided by (NIST, 2007). Once these have been obtained, the actual head produced by the pump is calculated as

$$\Delta H_a = \frac{\frac{P_d}{\rho_d} - \frac{P_s}{\rho_s}}{g} \times g_c + \frac{v_d^2}{2g} - \frac{v_s^2}{2g} \quad (11)$$

The discharge and suction fluid velocities are obtained from the mass flow rate as follows:

$$v_{d/s} = \frac{q_m}{\rho_{d/s} A_{d/s}} \quad (12)$$

In Equation (12), $A_{d/s}$ represents the cross-sectional area of the discharge and suction piping, respectively. The hydraulic power (in hp) produced by the pump is calculated from the following Equation (13):

$$HP = \frac{q_m}{\rho_d}\left(P_d - P_s + \frac{1}{2g_c}(\rho_d v_d^2 - \rho_s v_s^2)\right) \quad (13)$$

The thermodynamic efficiency of the pump is calculated from the actual enthalpy rise and the isentropic enthalpy rise. The actual enthalpy at suction (h_s) and discharge ($h_{d,a}$) conditions is calculated using measured temperature and pressure at the suction and discharge along with the property data. The measured suction temperatures were not used due to thermocouple errors and heat transfer to the environment through the body of the probe. Instead, saturation temperatures (and densities for saturated liquid) were obtained from (NIST, 2007) at each suction pressure. The isentropic discharge enthalpy ($h_{d,i}$) is calculated by first using tabular data to obtain the entropy of CO_2 at suction saturation conditions and then evaluating the enthalpy at the discharge pressure and suction entropy. The thermodynamic efficiency of the pump is equal to the ratio of isentropic enthalpy rise to actual enthalpy rise:

$$\eta = \frac{h_{d,i} - h_s}{h_{d,a} - h_s} \quad (14)$$

PUMP TEST RESULTS

The head versus flow performance behavior is shown in Figure 22 at three different speeds lines: 1,578 rpm, 2,500 rpm, and 3,510 rpm. The pump vendor provided factory test results using LN_2 for the nominal speed of 3,510 rpm whereas the other two speed lines were calculated using speed scaling laws. The comparison of both Tests 1 and 2 against the results provided by the pump OEM show very good correlation. The Pump performed well for both Tests 1 and 2, matching the measured performance during factory testing on LN_2. The comparison of predicted and measured head for the design point correlates within three percent for all tests. Notice that the pump was tested to flows well below that in the factory testing.

The pump efficiency was calculated based on actual power derived from energy balance calculations and isentropic power, as shown in Figure 23. Tests 1 and 2 show very good repeatability and correlation to the factory measurements on LN_2. While the efficiency values are relatively low compared to centrifugal compressors, the required pump power is an order of magnitude less than a comparable compressor as demonstrated by (Moore and Nored, 2008). Therefore the net power savings is still attractive.

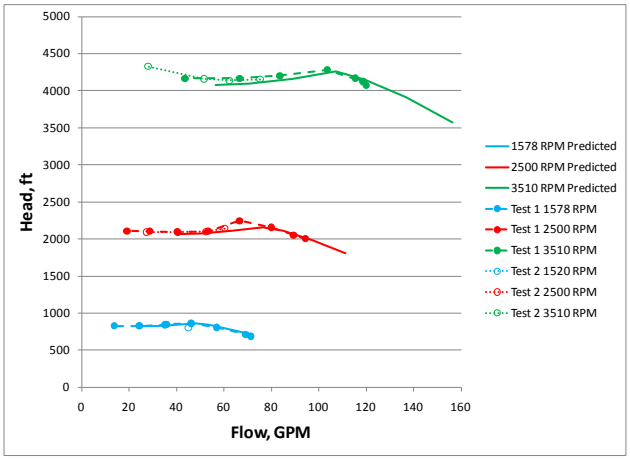

Figure 22. Pump Performance Plot (Head versus Flow)

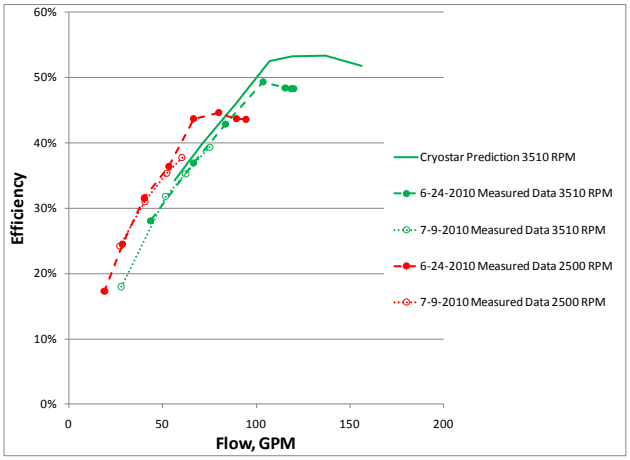

Figure 23. Pump Efficiency

The dynamic pressure measurement at the pump show little indication of unsteadiness for the design point as shown in Figure 24. The vibration levels observed during both tests were reasonable and did not exceed 0.2 inches per second (ips) (5.1 mm/sec) for the design flow operating point as shown in Figure

25. No subsynchronous pressure pulsations were encountered until operating well below (30 percent of) the design flow of the pump near the minimum NPSH.

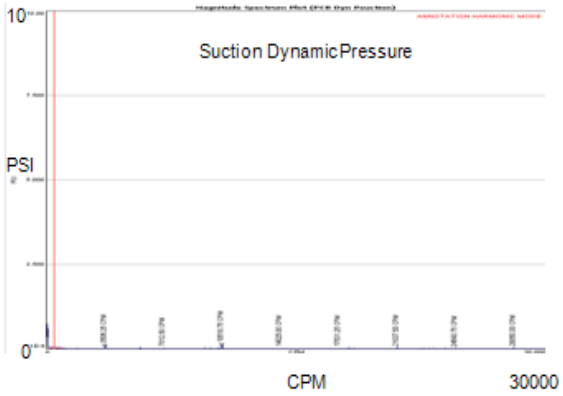

Figure 24. Suction Dynamic Pressure Spectrum for Design Operating Point

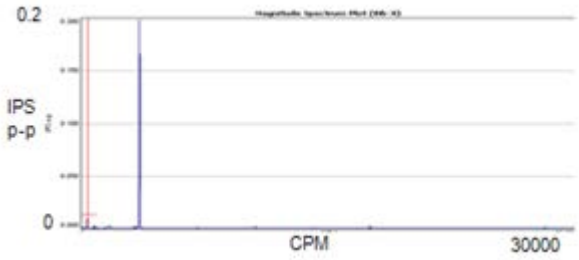

Figure 25. Pump Casing Vibration Spectrum for Design Operating Point

The pump was operated until the liquid level in the vessel reached the NPSH limit. No unusual pressure pulsations or vibration was observed.

CONCLUSIONS

All of the goals set forth in this test program have been accomplished. On the liquid CO_2 pump test program, an industrial cryogenic turbopump was adapted for service on CO_2. A new test facility was designed and fabricated and the pump was demonstrated to meet all project objectives in terms of both hydrodynamic and mechanical performance. For the internally-cooled compression concept, a cooling jacket was designed around a state of the art aerodynamic flow path that contained an optimal design of heat transfer enhancement without introducing additional pressure drop. An existing centrifugal compressor installed in a closed loop test facility was retrofitted with the new cooled diaphragm concept. The diaphragms were CNC machined and fabricated to provide accurate aerodynamic and cooling circuit geometry. The compressor was instrumented and tested per (ASME PTC-10, 1997). In addition, internal instrumentation was included to permit characterization of the stage performance, heat transfer, and pressure drop. The internally-cooled compressor tests demonstrated the effectiveness of the design, which exceeded expectations. Plans are being developed to construct a demonstration facility that would consist of an integrated multi-stage compression-liquefaction-pumping pilot plant.

NOMENCLATURE

C_d	=	Orifice plate coefficient of discharge [unitless]
d	=	Orifice plate bore diameter [inches]
D	=	Outside diameter of pipe [inches]
E	=	Quality factor from Table A-1A or A-1B of [4]
g	=	Acceleration due to gravity [in/s^2]
g_c	=	Unit correction factor = 32.174 lbm-ft/s^2/lbf
ΔH_a	=	Actual pump head [ft]
N_c	=	323.279 = Unit conversion for English units
ΔP	=	Orifice differential pressure [inches H_2O]
P	=	Internal design gage pressure [psi]
P_d	=	Discharge pressure [psi]
P_s	=	Suction pressure [psi]
q_m	=	Mass flow rate [lbm/sec]
S	=	Stress value for material from Table A-1 of [4]
T	=	Pressure design thickness [inches]
v_d	=	Fluid velocity at discharge [ft/s^2]
v_s	=	Fluid velocity at suction [ft/s^2]
Y	=	Expansion factor (= 1.0 for liquid), unitless
Y	=	Coefficient taken from Table 304.1.1 of [4]
β	=	Diameter ratio, unitless
$\rho_{t,p}$	=	Density upstream of the orifice [lbm/ft^3]
ρ_d	=	Discharge density [lbm/ft^3]
ρ_s	=	Suction density [lbm/ft^3]

REFERENCES

ASME, B31.3, 2002, Process Piping Design Standard, American Society of Mechanical Engineers, New York, NY.

ASME, PTC 8.2, 1990, Power Test Code for Centrifugal Pumps, American Society of Mechanical Engineers, New York, NY.

ASME, PTC 10, 1997, Performance Test Code on Compressors and Exhausters, American Society of Mechanical Engineers, New York, NY.

Cengel, Y. A., 2003, "Heat Transfer: A Practical Approach," 2nd. Ed., McGraw-Hill, New York, NY, 2003.

Han, J. C., 2006, "Turbine Blade Cooling Studies at Texas A&M University: 1980-2004," Journal of Thermophysics and Heat Transfer, Vol. 20, No. 2, April-June 2006, pp. 161-187.

Herzog, H. J., 1997, "CO_2 Capture, Reuse, and Sequestration Technologies For Mitigating Global Climate Change," Advanced Coal-Based Power and Environmental Systems Conference, Pittsburgh, PA (United States), July 22-24, 1997.

Moore, J. J., Nored, M.B., 2008, "Novel Concepts for the Compression of Large Volumes of Carbon Dioxide," GT2008-50924, ASME Turbo Expo 2008: Power for Land, Sea and Air, June 9-13, 2008 in Berlin, Germany.

MPMS Chapter 14.3.4, 2002, Concentric, Square-edged Orifice Meters – Part 4 – Background, Development, Implementation Procedures and Subroutine Documentation, 3rd Edition, American Petroleum Institute, Washington, D.C.

NIST, 2007, NIST Reference Fluid Thermodynamic and Transport Properties - REFPROP, Version 8.0, Physical and Chemical Properties Division, National Institute of Standards and Technology (NIST), Boulder, Colorado 80305, April 2007.

Ridouane, E. H. and Campo, A., 2008, "Heat Transfer Enhancement of Air Flowing Across Grooved Channels: Joint Effects of Channel Height and Groove Depth," Journal of Heat Transfer, Vol. 130, February 2008.

ACKNOWLEDGEMENTS

The authors would like to thank the National Energy Technology Laboratory (NETL) within the United States Department of Energy (DOE) for providing the majority of the funding for this work and Dresser-Rand and BP for the additional co-funding required.